Friction stir welding of laser-powder bed fusion A20X: microstructure and mechanical properties

Original
Friction stir welding of laser-powder bed fusion A20X: microstructure and mechanical properties / Abankar, M., Lunetto, V., De Maddis, M., Lombardi, F., Razza, V., Russo Spena, P.. - In: PERIODICA POLYTECHNICA. MECHANICAL ENGINEERING. - ISSN 0324-6051. - ELETTRONICO. - (2024). [10.3311/PPme.38444]

Publisher:
Faculty of Mechanical Engineering of the Budapest University of Technology and Economics

Published
DOI:10.3311/PPme.38444

Materials Today Communications 51 (2026) 114894

Contents lists available at ScienceDirect

Materials Today Communications

journal homepage: www.elsevier.com/locate/mtcomm

Topographical and mechanical properties of sputtered composite coatings with silver nanoparticles for functional surfaces

Lorenzo Giorio [a], Giacomo Maculotti [a,*], Francesca Gattucci [b], Gianfranco Genta [a], Cristina Balagna [b], Maurizio Galetto [a]

[a] *Department of Management and Production Engineering, Politecnico di Torino, Corso Duca degli Abruzzi 24, Turin 10129, Italy*

[b] *Department of Applied Science and Technology, Politecnico di Torino, Corso Duca degli Abruzzi 24, Turin 10129, Italy*

ARTICLE INFO

Keywords:
Thin coatings
Co-sputtering
Composite
Nanoindentation

ABSTRACT

The development of durable, effective functional coatings is a pressing challenge in biomedical and surface engineering applications. This work investigates the morphological, topographical, and mechanical properties of nanocomposite coatings functionalized by silver nanoparticles (Ag NPs) embedded in SiO_2 and ZrO_2 matrices, deposited by co-sputtering. The effects of matrix material and deposition duration are investigated in terms of their impact on composition, morphology, topography and mechanical response, which are tested, respectively, by EDS, FESEM, conductive AFM, topographical microscopy and nanoindentation. Results show a complex combined effect of nano structure and average structural and topographical properties and composition on the mechanical response. Results highlight that for longer depositions, average properties are controlled by micro-scale topography and average structure and composition. Conversely, for shorter depositions, local structural differences strongly influence the average mechanical response and result in a greater dispersion of the mechanical properties. These findings demonstrate the tunability of coating properties through process control. Future research will apply these insights to optimize the functionality of fibers and textiles.

1. Introduction

Surfaces of medical tools, food packaging, frequently touched items, fabrics, and air filtration systems are vulnerable to microbial contamination, which undermines their performance and durability on a global scale [1]. This contamination also plays a critical role in the escalation of antimicrobial resistance (AMR) worldwide [2]. A major driver of this crisis is the excessive or inappropriate application of antimicrobial agents in both human and veterinary contexts [3], emphasizing the importance of effective strategies to curb bacterial spread [4].

Silver is widely acknowledged for its strong antimicrobial properties in both ionic and nanoparticle form [5]. Although the exact antibacterial mode of action of silver nanoparticles (Ag NPs) remains under investigation, two primary mechanisms are suggested: the emission of silver ions and the intrinsic chemical activity of the nanoparticles themselves. Ag NPs can breach bacterial membranes, leading to cellular destruction, while released silver ions interfere with essential processes such as ATP synthesis and DNA replication. These ions also stimulate the production of reactive oxygen species (ROS), which further contribute to bacterial eradication [6]. On the antiviral front, although the precise pathways are not fully defined, Ag NPs have demonstrated significant efficacy against a variety of viruses, including SARS-CoV-2 [7].

To enhance the advantages offered by silver nanoparticles (Ag NPs) while simultaneously minimizing their potential toxicity, uncontrolled release, and environmental buildup, they are frequently incorporated into various matrices or coatings. Embedding Ag NPs within an inorganic SiO_2 or ZrO_2 matrix stabilizes the nanoparticles by reducing their direct exposure to the environment and limiting uncontrolled particle release, while enabling a more controlled and durable antimicrobial functionality [8].

Physical Vapor Deposition (PVD) is a widely used technique for applying uniform and adherent coatings to various substrates, including heat-sensitive ones like electrospun fibers and textiles [9]. This technique involves vaporizing a solid material under vacuum conditions and condensing it onto a substrate, enabling precise control over the film's thickness and composition [10]. In particular, sputtering and evaporation methods are favored in large-scale applications due to their high deposition rates and ability to coat substrates of diverse shapes and

---

* Corresponding author.
E-mail address: giacomo.maculotti@polito.it (G. Maculotti).

https://doi.org/10.1016/j.mtcomm.2026.114894
Received 17 September 2025; Received in revised form 17 February 2026; Accepted 19 February 2026

geometries [11].

The technique of co-sputtering is a PVD method that allows the deposition of composite coatings embedding silver nanoparticles [12]. Ferraris et al. introduced a patented surface treatment incorporating silver nanoclusters dispersed in a ceramic or glass-based matrix [12,13]. These coatings, obtained via co-sputtering, have consistently demonstrated remarkable antibacterial [12] and antiviral [13,14] performance, and have been successfully applied to thermally sensitive substrates such as cotton textiles [15] and air filters [16].

Co-sputtering is a versatile method for producing nanocomposite coatings with customized properties, showing strong potential for scale-up. Its current use in industry for covering extensive surfaces, including architectural glass, highlights its suitability for wider adoption in fields where antimicrobial performance is essential [17].

To be practical for industrial-scale use, antimicrobial coatings (AMCs) must retain their functional integrity over extended periods and under varying operational conditions. The mechanical behavior, such as their ability to resist wear and physical stress, of these coatings is a key factor in ensuring long-term reliability. Additionally, it is important to evaluate how the coating alters the texture of the surface, as smoother surfaces can inhibit microbial attachment and improve overall cleanliness [18].

The mechanical performance of antibacterial coatings plays a vital role in their applicability across different fields, including medical implants and textiles. These properties directly affect how well the coatings endure stress, retain functionality, and adapt to the physical demands of the target substrate [19]. For instance, in orthopedic implants, coatings must resist mechanical loads without compromising their antimicrobial action [20], while in textile applications, they must maintain the material's natural flexibility and breathability to ensure comfort and usability [21].

In this context, surface roughness also plays a pivotal role [22]. When evaluating the suitability of an antibacterial coating for a specific substrate, it is essential to consider how the deposition process alters the surface morphology. Depending on the nature of these changes, the coating may enhance or hinder antibacterial effectiveness by either discouraging or promoting bacterial attachment [23].

While the antibacterial efficacy of silver nanoparticle-based composite coatings has been well established in previous studies, less attention has been given to the detailed analysis of their surface and mechanical properties, which are critical for practical deployment. This work, focusing on sputtered composite coatings made of a silica or a zirconia matrix embedding silver nanoparticles, deposited via co-sputtering, presents a comprehensive characterization of their morphology, surface topography, and mechanical behavior. This study aims to provide insights into co-sputtered antibacterial coatings structural uniformity, surface roughness, and mechanical robustness, key factors in determining their suitability for industrial and biomedical applications.

The rest of the paper is structured as follows. Section 2 presents the investigated materials, highlighting the manufacturing conditions and the characterization methods. Section 3 presents the results of the characterization, and Section 4 discusses the obtained results. Finally, Section 5 draws conclusions.

2. Materials and methods

This work aims to investigate the effect of co-sputtering process parameters on surface morphology and mechanical properties of antibacterial coatings. Accordingly, a full factorial design [24] was implemented to investigate the effects of the matrix material, i.e. SiO_2 or ZrO_2, and deposition duration, i.e. 30 min and 60 min, on the manufactured coating. Three batches per manufacturing condition were produced to cater for process reproducibility.

2.1. Coating deposition

The coatings comprise silver nanoparticles embedded in both silica and zirconia matrices, deposited onto silicon wafer substrates using a patented co-sputtering technique [13]. The sputtering system was equipped with two targets for each deposition: for the silica-based coating, a high-purity silica target (Sigma-Aldrich, 99.99 %) and a silver target (Franco Corradi S.r.l., 99.9 %); for the zirconia-based coating, a zirconia target (Nanovision™, 99.98 % ZrO_2) and the same silver target.

The sputtering power settings were as follows:

- Silica-based coating: 200 W in radio frequency (RF) mode for the silica target and 5 W in direct current (DC) mode for the silver target.
- Zirconia-based coating: 250 W in RF mode for the zirconia target and 4 W in DC mode for the silver target.

All depositions were conducted in a pure argon atmosphere at a pressure of 5.5 dPa for 30 min and 60 min. The deposition parameters were chosen based on previous studies [16,19]. The antimicrobial functionality of analogous Ag-nanocluster composite coatings produced by co-sputtering has been demonstrated in previous works. Both SiO_2-Ag and ZrO_2-Ag coatings exhibited significant antibacterial activity against Gram-negative and Gram-positive bacteria on rigid substrates and on textile materials [12,14,16,26,27]. The same coating architecture showed antiviral efficacy, including complete inactivation of SARS-CoV-2 on coated respirators and virucidal activity against human coronavirus on fibre-based filter media [15,16].

Compositional analysis was performed using energy-dispersive spectroscopy (EDS; EDAX PV 9900TM) to identify the elemental makeup of the coatings, which plays a key role in influencing their mechanical behavior. The analysis was performed at low magnification (500 ×), with the mean concentration determined from measurements taken in three separate areas.

2.2. Morphological characterization

Morphological characterization of the coatings was carried out using a field emission scanning electron microscope (FESEM; QUANTA INSPECT 200 and Zeiss SUPRA 40) at 200k× of magnification to observe and compare surface features. Imaging was conducted using an in-lens secondary electron detector to enhance resolution and surface detail. The magnification was selected to obtain sufficient resolution of features and a field of view comparable with atomic force microscopy. The morphology of the coatings was additionally analysed in cross-section at 50k× magnification, in order to assess the vertical development of surface features.

Atomic Force Microscopy in conductive mode (C-AFM) was performed. C-AFM is a contact AFM technique which allows measuring the current flowing through the sample and the cantilever tip, provided the application of an electric potential. Thus, C-AFM associates the topographical height signal with a current signal. Measurements were performed by applying 10 V and inspecting three random locations. Per each location, a $(500 \times 500)\ \mathrm{nm}^2$ area with a lateral resolution of 1 nm was measured. C-AFM was performed to investigate surface layer properties depending on the morphology highlighted by FESEM analysis. AFM inspected areas were designed to obtain a magnification similar to the highest of FESEM magnification.

2.3. Surface topography characterization

Surface topography was measured by means of a Phase Shifting Interferometer (PSI) [28,29] Sensofar Sneox equipped with a 50× magnification Mirau objective (numerical aperture 0.55, squared pixel size of 0.28 μm). The instrument was calibrated, showing a measurement noise of 0.1 nm, a flatness deviation of 4.9 nm, and z-axis linearity of 1 nm [30]. Six random fields of view (FoV) of (280.6 × 280.6) μm^2 per sample were measured. Scale-limited (SL) surface was characterized after the application of a form-removal operator (F-operator), implemented as the subtraction of the least-square evaluated plane, and of robust gaussian S-filter and L-filter, respectively, with nesting index of $N_{is} = 1$ μm and $N_{ic} = 100$ μm [31,32]. The SL-surface was characterized in terms of surface height parameters, namely, the arithmetic mean height Sa, the root mean square height Sq, the skewness Ssk, the kurtosis Sku, the maximum pit depth Sv, the maximum peak height, and the maximum height Sz (indicating the topography range) [31]. The application of standard operators, i.e. the processing sequence of F-operator, S-filter and L-filter, and the evaluation of the topographical parameters was carried out by MountainsLab v8.1 [33].

2.4. Mechanical characterization

Mechanical characterization of the coating was performed by instrumented indentation test (IIT), also known as nanoindentation [34]. IIT applies a force-controlled loading-holding-unloading cycle to a sample by means of an indenter and, throughout the test, measures the applied force F and the indenter penetration h. The analysis of the resulting indentation curve, i.e. $F(h)$, allows evaluating the indentation hardness H_{IT} and the indentation modulus E_{IT}, which estimates the Young's modulus. To obtain the mechanical response of the coating, separating the effect of the substrate [35], this work applied the ISO 14577–4 methodology [36]. The required indentations at increasing depth were obtained by means of an in-depth characterization performed by applying 25 subsequent indentation cycles with an increasing maximum force in the same point [37]. Indentations were performed by means of an Anton Paar NHT^3 nanoindentation machine. The machine was calibrated and has an indentation modulus relative measurement uncertainty of 2 % [38,39]. Each indentation cycle consisted of a loading and unloading of 10 s and a holding of 15 s. The maximum force was quadratically spaced in a range from 0.1 mN to 25 mN. Per each sample, a 4 × 4 matrix of indentations with a 50 μm spacing was performed for evaluating reproducibility. To separate the effect of the substrate the ISO 14577–4 methodology was applied [37], and the coating thickness was obtained by statistical deconvolution [40].

3. Results

3.1. Compositional analysis

The elemental composition of the SiO_2Ag and ZrO_2Ag coatings was assessed by energy-dispersive X-ray spectroscopy (EDS), and the results are summarized in Table 1. In all samples, silicon is the most abundant element detected. However, since the coatings were deposited on Si wafers and are relatively thin, the silicon signal partially originates from the substrate. This is a common occurrence in EDS analysis of thin films, as the information depth of EDS typically ranges from several hundred nanometers to few micrometers, depending on the accelerating voltage and material density [41], which may result in substrate contributions when analyzing coatings with nanometric thicknesses.

In the SiO_2-based coatings, the atomic percentage of silver increases significantly with deposition time, from (1.67 ± 0.06) at% in the 30 min deposition sample to (3.90 ± 0.20) at% after 1 h. In the ZrO_2-based coatings, silver content also increases with deposition time, from (0.97 ± 0.12) at% to (1.91 ± 0.02) at%, along with an increase in zirconium content.

3.2. Morphological characterization

The surface morphology of co-sputtered SiO_2- and ZrO_2-based coatings was investigated by field-emission scanning electron microscopy (FESEM), as shown in Fig. 1. FESEM morphological investigation aimed to assess the influence of deposition time and matrix composition on the film structure.

The SiO_2-based coating deposited for 30 min, see Fig. 1a), exhibited a compact nanoparticulate morphology, consisting of closely packed nanoscale clusters. A few isolated, larger clusters were observed across the surface, suggesting localized accumulation during growth. With a deposition time of 1 h, see Fig. 1b), the number and size of larger clusters increased significantly, with enhanced particle growth or coalescence over time, indicating a morphological evolution toward more heterogeneous surfaces. In addition, the coating in Fig. 1b) appears significantly more porous than that in Fig. 1a), likely due to the accumulation of loosely packed nanoparticles during the extended deposition time.

In contrast, the ZrO_2-based coating deposited for 30 min, see Fig. 1c), exhibited a distinctly different morphology, characterized by the presence of elongated surface structures distributed across the coating. These features indicate the early development of crystalline domains, a behavior also observed by Luceri et al. upon co-sputtering ZrO_2-based systems [25]. After 1 h of deposition, see Fig. 1d), larger surface formations emerged. This led to a hierarchical morphology, combining both well-defined crystalline features and irregularly shaped clusters.

Figs. 2 and 3 report, respectively, the results of conductive AFM on SiO_2 and ZrO_2 based coatings. Comparison of the topography and current signal highlights that the highest conductivity is in correspondence with topographical hills, thus suggesting that the protruding features, well highlighted in FESEM analysis, are due to clusters containing Ag NPs. As far as conductivity is concerned, the current ranges are highly informative. It can be noticed that the current range increases of a half order of magnitude only for SiO_2+Ag NPs with deposition duration, i.e. from 0.2 nA to 0.6 nA, whilst it remains almost constant for ZrO_2+Ag NPs (0.03 nA). Also, the current range of SiO_2+Ag NPs is at least one order of magnitude larger than range of ZrO_2+Ag NPs, indicating a greater conductivity of the silica-based coating.

3.3. Surface topography characterization

Fig. 4 shows the measured surface topographies of the coatings in the four considered processing conditions. Qualitatively, it can be appreciated the larger surface height range for SiO_2-based coatings, and the presence of topographical hills. Surface topography areal field height parameters of the SL-surface were computed as described in Section 2.3, and interval plots are reported in Fig. 5. Interval plots show an average decrease of the roughness for longer deposition duration for SiO_2-based coatings. Also, dispersion of main topographical parameters, i.e. Sa, Sq, is smaller for ZrO_2-based coatings, indicating a more homogeneous topography over the five investigated areas. Mean and standard deviation of the evaluated topographical parameters (shown in Fig. 5) are also

Table 1
EDS results. Weight (%wt) and atomic (%at) relative composition of the four considered composite coatings. The reported dispersion is expanded uncertainty (k = 2).

Element	Si		Zr		O		Ag	
Sample	% wt	% at	% wt	%at	% wt	%at	%wt	%at
SiO_2+Ag NPs 30 min	87.64 ± 0.26	87.85 ± 0.28	-	-	5.96 ± 0.16	10.48 ± 0.28	6.40 ± 0.24	1.67 ± 0.06
SiO_2+Ag NPs 60 min	76.85 ± 0.42	80.05 ± 1.16	-	-	8.78 ± 0.84	16.01 ± 1.32	14.37 ± 0.62	3.90 ± 0.20
ZrO_2+Ag NPs 30 min	87.28 ± 0.46	91.05 ± 0.32	5.82 ± 0.38	1.87 ± 0.12	3.34 ± 0.20	6.12 ± 0.34	3.56 ± 0.40	0.97 ± 0.12
ZrO_2+Ag NPs 60 min	80.26 ± 0.30	86.23 ± 0.40	8.04 ± 0.12	2.66 ± 0.04	4.88 ± 0.20	9.21 ± 0.36	6.81 ± 0.04	1.91 ± 0.02

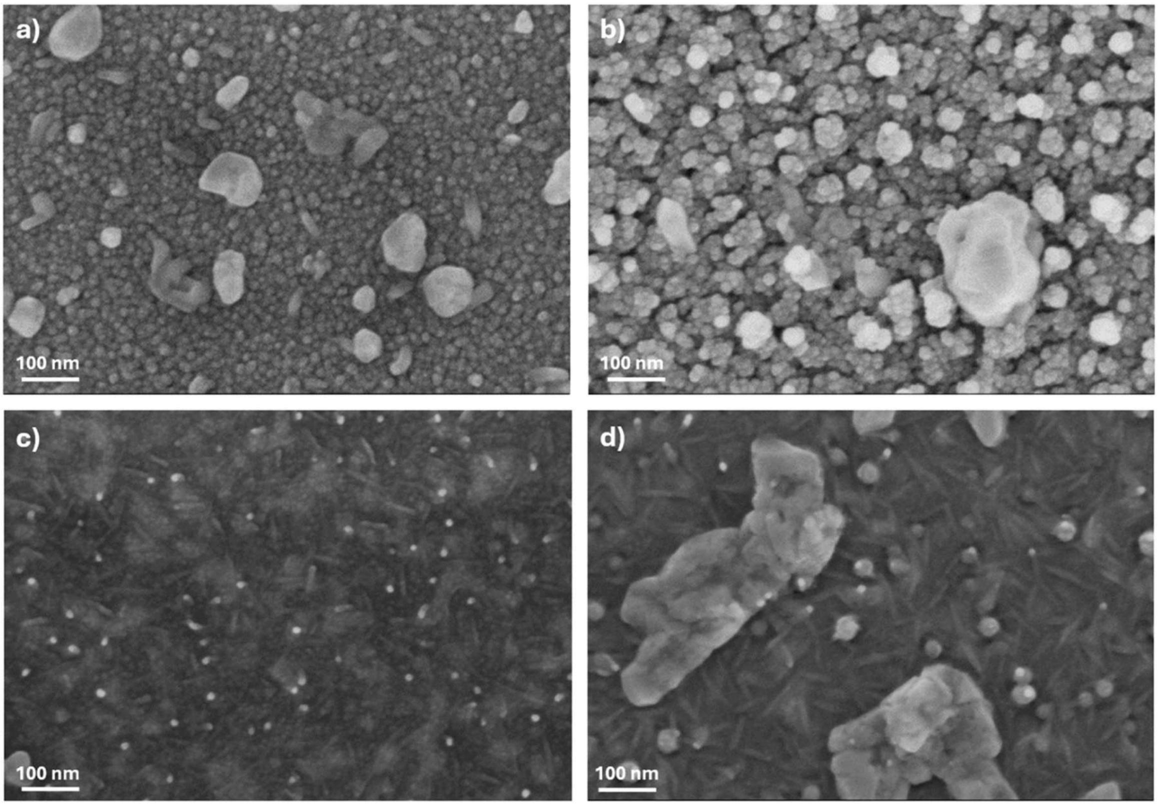

Fig. 1. FESEM morphological analysis of the considered coating: a) SiO_2+Ag NPs with deposition duration of 30 min, b) SiO_2+Ag NPs with deposition duration of 60 min, c) ZrO_2+Ag NPs with deposition duration of 30 min, d) ZrO_2+Ag NPs with deposition duration of 60 min. Magnification of 200k× .

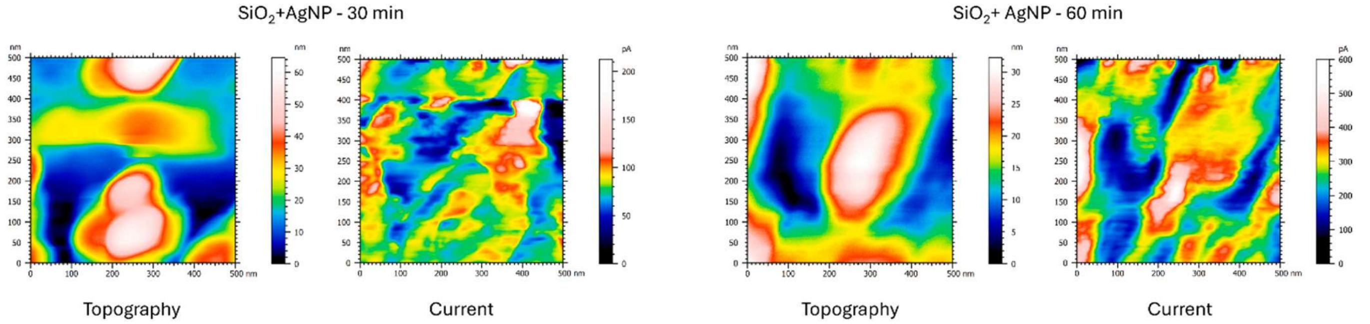

Fig. 2. Conductive AFM on SiO_2+Ag NPs for deposition of 30 min (left) and 60 min (right). Topography and current signal are reported. Notice the higher conductivity at hills and hills' edges.

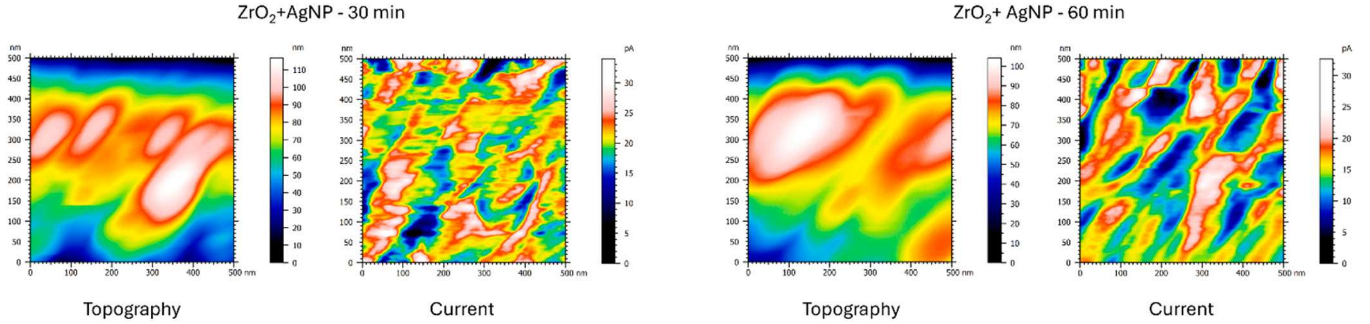

Fig. 3. Conductive AFM on ZrO_2+Ag NPs for deposition of 30 min (left) and 60 min (right). Topography and current signal are reported. Notice the higher conductivity at hills and hills' edges.

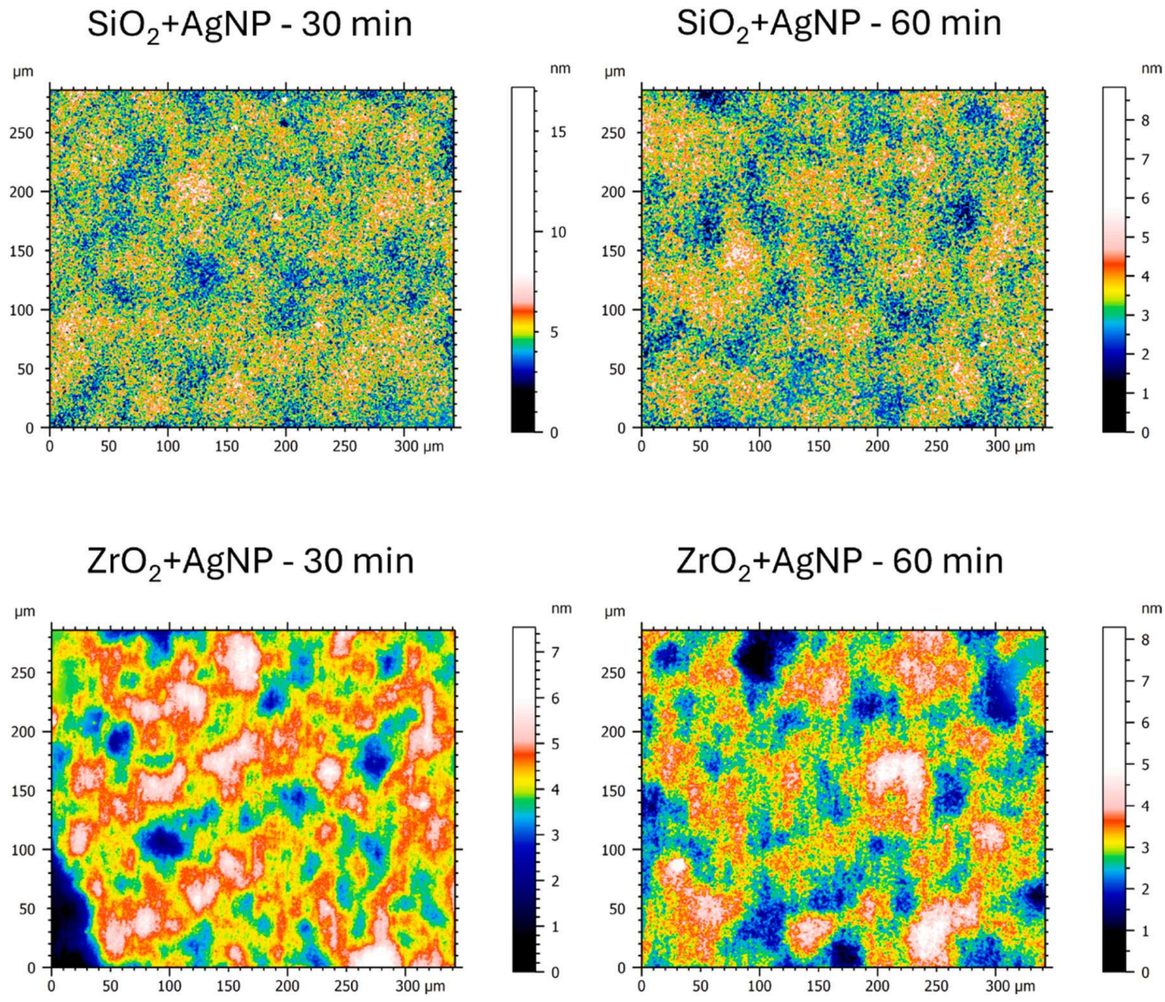

Fig. 4. Measured SL-surface topographies of considered antibacterial coatings. Pseudo colours maps. Notice the rougher topography of SiO_2 based coatings.

reported in Table 2.

Investigation of main and interaction plots, respectively shown in Figs. 6 and 7, allows qualitatively appreciating the effects of matrix material and deposition duration on the average of evaluated surface topography parameters. In particular, ZrO_2-based coatings are smoother (Sa, Sq), with a more limited height range (Sp, Sv, Sz). Main effects plots in Fig. 6 highlight that longer depositions yield a smoother surface, even though the effect is more limited than the one due to the matrix material. Formal quantitative investigation was provided by ANOVA [24]. Synthetic results are summarized in Table 3 and highlight that for Sa, Sq, Sp and Sz both the matrix material and the deposition process duration and their interaction produce systematic variations on the topographical parameters, i.e, they are significant. For Sv, the interaction between the matrix material and the deposition process duration does not significantly affect the topography, while for Ssk and Sku, only the matrix material significantly affects the topography.

Interaction plots in Fig. 7 allow insights into the results obtained. In particular, they show that SiO_2-based coating is more sensitive to the co-sputtering duration, highlighting the significant interaction between the matrix material and the process duration. Also, the interaction plot for Sv shows that a longer deposition tends to produce shallower dales, regardless of the material, motivating why the interaction effect cannot be considered significant for Sv. Conversely, for Sp the interaction between the matrix material and the deposition duration is significant, and, as can be seen from the relevant interaction plot, shorter hills are generated on SiO_2-based coating, taller hills for ZrO_2, for longer durations. Last, interaction plots for Ssk and Sku show that a longer deposition duration produces a surface topography approaching a normal distribution (Ssk ~ 0 and Sku ~ 3). Further insights from pairwise hypothesis test on the mean (*t*-test), graphically shown in Fig. 5, highlight that no significant improvement is obtained for ZrO_2-based coatings at longer deposition. Also, despite the overall improvement, the SiO_2-based coating is still rich of dales (Ssk statistically larger than 0).

3.4. *Mechanical characterization*

Mechanical characterization was performed by nanoindentation test as per the methodology described in Section 2.4 [36]. Thickness of the coating was measured by statistical deconvolution of the mechanical response [40] resulting in an average thickness of (97.8 ± 22.7) nm, (169.0 ± 20.8) nm respectively for SiO_2+Ag NPs with a sputtering duration of 30 min and 60 min, and of (53.7 ± 8.8) nm, and (117.8 ± 15.1) nm, respectively for ZrO_2+Ag NPs with a sputtering duration of 30 min and 60 min. The indentation produced at the lowest maximum force, i.e. 0.1 mN, showed an average side length in the order of 100 nm. Thus, considering the dimensions of morphological and functional features, presented in Section 3.2, the mechanical characterization provides an average of the matrix and the functionalizing NPs. Fig. 8 shows the mechanical characterization results for the coating. Uncertainty of the measurement combines the coating morphological and structural dispersion due to manufacturing and the uncertainty of the standard method for the substrate effect deconvolution. Pairwise comparisons are performed based on hypothesis test on the t-Student distribution with a risk of error of 5 %. Indentation modulus (E_{IT}) results, shown in Fig. 8a),

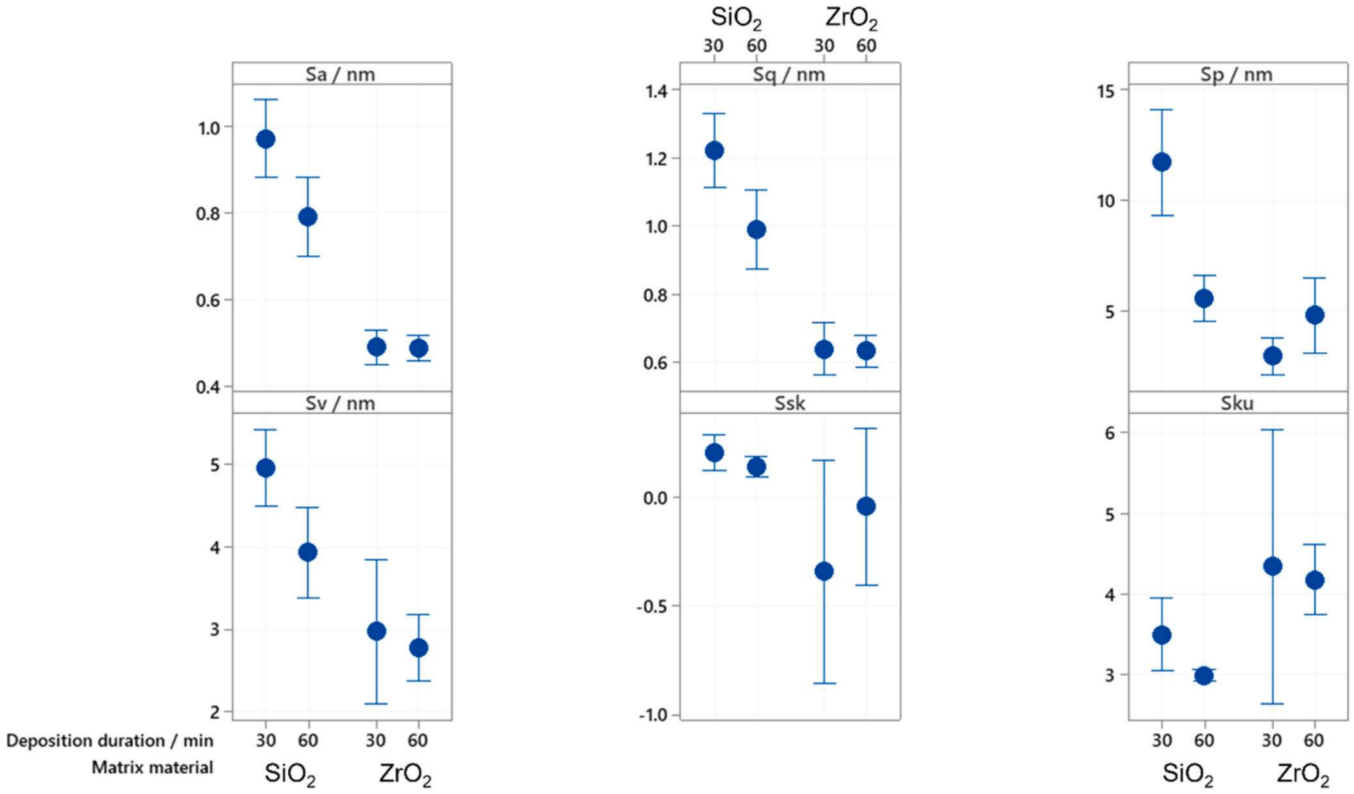

Fig. 5. Interval plots of SL-surface height parameters of the considered coating. Sz is not shown as it is the sum of Sp and Sv. Error bars show 95 % confidence intervals for the sample average.

Table 2
Mean (*m*) and standard deviation (*s*) of the considered surface topography parameters for the four different processing conditions.

	SiO_2 Ag NPs 30'		**SiO_2 Ag NPs 60'**		**ZrO_2 Ag NPs 30'**		**ZrO_2 Ag NPs 30'**	
	m	*s*	*m*	*s*	*m*	*s*	*m*	*s*
Sa / µm	0.971	0.086	0.790	0.088	0.489	0.038	0.486	0.029
Sq / µm	1.221	0.104	0.988	0.109	0.638	0.073	0.632	0.045
Sp / µm	11.692	2.260	5.558	1.003	2.937	0.804	4.789	1.609
Sv / µm	4.690	0.440	3.930	0.519	2.973	0.829	2.783	0.383
Ssk / -	0.203	0.080	0.140	0.044	-0.343	0.049	-0.044	0.0344
Sku / -	3.497	0.432	2.995	0.072	4.343	1.616	4.177	0.410

allow appreciating that the process duration does not affect the stiffness of the SiO_2-based coating. Conversely, a significant increase of the stiffness of the ZrO_2-based coating is obtained for longer deposition, producing a coating significantly stiffer than the SiO_2+Ag NPs. Average indentation hardness (H_{IT}) response, shown in Fig. 8b), highlights that ZrO_2 matrix allows obtaining harder coatings. The process duration effect is peculiar. In fact, longer depositions do not induce any significant effect on the ZrO_2-based coatings' hardness, whilst a softening is shown for SiO_2 matrix. It is also interesting to point out that longer depositions reduce the measurement uncertainty; also, ZrO_2-based coatings show more dispersed mechanical properties.

4. Discussion

The results underscore the critical influence of matrix composition and deposition time on the morphological, topographical, and mechanical properties of SiO_2- and ZrO_2-based coatings functionalized by Ag NPs-containing. EDS analysis confirms that prolonged deposition increases ZrO_2 content in the composite, reflecting progressive matrix growth over time. Similarly, the functional particle content increases almost linearly, regardless of the matrix material, with deposition duration (see Table 1). Likewise, the coating thickness tends to progress linearly with process duration; particularly, ZrO_2-based coatings are thinner for the same deposition duration.

FESEM images reveal distinct morphological evolutions: SiO_2 coatings become markedly more porous for longer deposition, likely due to the aggregation of loosely packed nanoparticles, while ZrO_2 coatings exhibit semicrystalline domains, with larger and more defined clusters forming at extended durations. Conductive AFM measurements showed the electrical behaviour of the coatings, complementing the morphological characterization obtained by FESEM. In particular, SiO_2-based coatings consistently exhibit higher conductivity than ZrO_2-based coatings, with an order of magnitude difference in the measured current range, which is reasonably attributed to SiO_2 intrinsically lower resistivity. Notably, only SiO_2-based coatings show a significant increase in current with deposition time, due to the increase of Ag content. Conversely, the lack of current range variation with deposition duration for ZrO_2-based coatings can be explained by the concurrent increase in ZrO_2 fraction, which strongly limits any enhancement from the growing Ag NPs clusters. Additionally, the locally higher current measured in correspondence with topographical hills strongly suggests that such hills, which at FESEM inspection appear as clusters, are richer in Ag NPs than the rest of the surface.

Surface topography analysis indicates that prolonged deposition

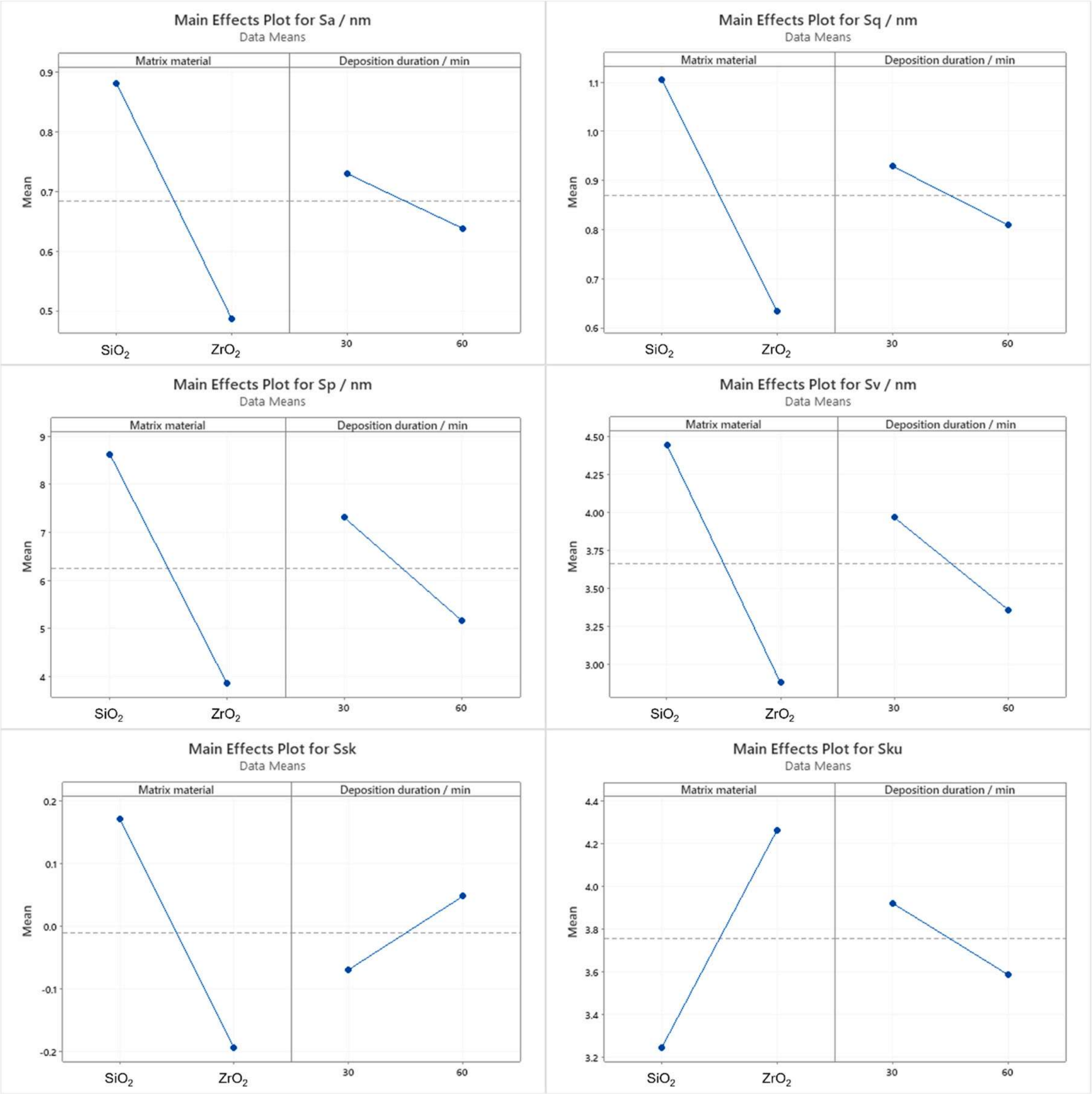

Fig. 6. Main effects plot of SL-surface topography parameters. For each parameter, it represents the average of all measurements having the characteristic indicated by the label. Sz is not shown as it is the sum of Sp and Sv.

leads to smoother and more homogeneous surfaces across both matrices. For SiO_2-based coatings, a reduction in both the average and dispersion of parameters (e.g., Sa, Sq) is observed, while for ZrO_2-based coatings, surface uniformity improves across inspected areas, albeit maintaining isolated clusters. The increase in cluster size, coupled with infill of surface dales, results in reduced peak (Sp) and valley (Sv) depths, indicating a general homogenization of the surface. This is confirmed by higher-order topographical surface height field parameters (Ssk, Sku), which reveal a trend toward symmetry with longer deposition durations. For SiO_2 matrix, Ssk decreases toward zero, suggesting a reduction in surface dales, a trend corroborated by decreases in Sv and supported by FESEM and AFM observations of larger but more evenly distributed clusters. For ZrO_2 matrix, dominated by isolated high peaks ($Sku > 3$) for the shorter deposition, the surface also shifts toward a more balanced topography, though high Sp values persist due to vertically extensive cluster growth.

Mechanical characterization confirms that, given the indentation scale (in excess of 100 nm in the lateral direction) with respect to the coating microstructure, the measured values represent an averaged mechanical response between the matrix and the NPs. The overall reduction in measurement uncertainty with deposition time reflects the effect of smoother topographies for longer depositions. In particular, a large variability is observed in ZrO_2+Ag NPs for 30 min deposition. In the ZrO_2-based coating, the Ag content is very low, as indicated by EDS analysis in Table 1, and distributed in very sparse and isolated clusters, which are richer in Ag, as highlighted by conductive AFM analysis. Ag exhibits elastic modulus and hardness values smaller by an order of magnitude than those of ZrO_2. The randomly located indentation measurements result of a mixture of regions containing Ag NPs and regions poorer with Ag content, resulting in a significant increase of data dispersion. The increase of the Ag fraction (as measured by EDS) should worsen the situation. However, it is evident that the increased coating thickness plays a dominant role, leading to a more uniform film mechanical response. In any case, the mechanical response dispersion for ZrO_2-based coating (even for 60 min deposition) remains significantly higher than that observed for SiO_2 matrix. Since surface roughness does not account for this phenomenon, composition appears to be the only plausible explanation. Conversely, in terms of average mechanical response, the substantially different microstructure and morphology, highlighted in previous analyses, lead to diverse mechanical response

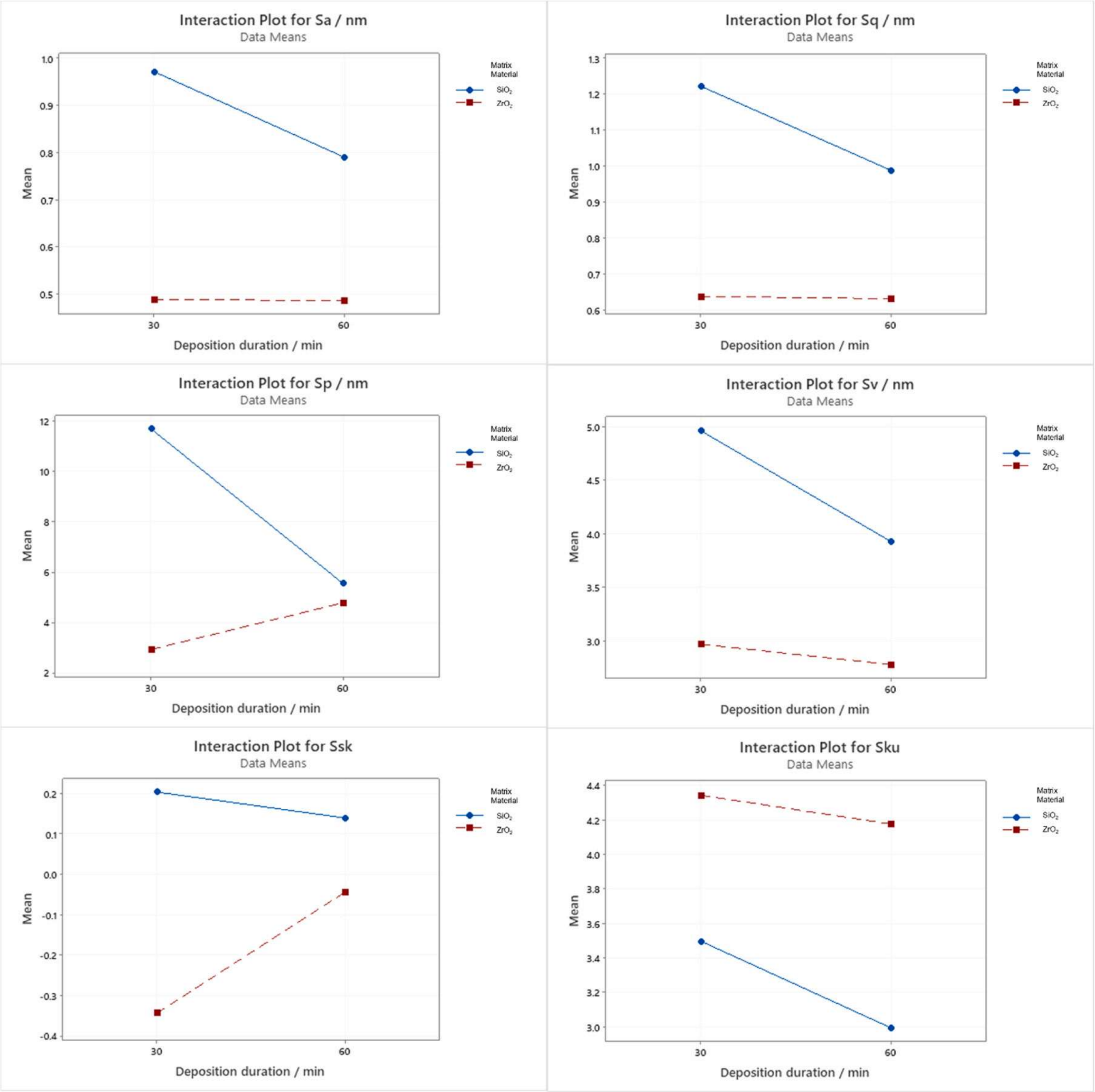

Fig. 7. Interaction plot of SL-surface topography parameters. For each parameter, it represents the average of measurements on coatings deposited with same process duration, parametrized by the matrix material (blue SiO_2, and red ZrO_2). Sz is not show as it is the sum of Sp and Sv.

Table 3
p-values of factors and their interaction effect on topographical height parameters evaluated by ANOVA. P-values smaller than 0.05 indicates a significant systematic effect of the factor or the interaction on the parameter at a confidence level of 95 %.

Parameter	Matrix Material	Deposition Duration	Matrix Material * Deposition Duration
Sa	< 0.001	0.003	0.003
Sq	< 0.001	0.003	0.004
Sp	< 0.001	0.003	< 0.001
Sv	< 0.001	0.016	0.086
Sz	< 0.001	< 0.001	< 0.001
Ssk	0.008	0.352	0.157
Sku	0.009	0.354	0.638

changes due to process duration (formally confirmed by ANOVA). Specifically, for ZrO_2-based coatings, a significant increase in indentation modulus (E_{IT}) is observed with longer deposition, attributable to greater coating thickness. For SiO_2 matrix, a reduction in hardness (H_{IT}) for 60 min deposition aligns with the observed increase in porosity and greater Ag content, as evidenced by FESEM and EDS, both of which are liable of a decrease in hardness.

5. Conclusions

This work studies the morphological and mechanical properties of ceramic matrix composite coating incorporating Ag NPs deposited by co-sputtering. This work showed the significant impact of matrix material and deposition duration on the morphological, topographical, and mechanical properties of SiO_2+Ag NPs and ZrO_2+Ag NPs coatings. Prolonged deposition enhances ZrO_2 content and promotes semicrystalline growth, while in SiO_2 matrix it leads to increased porosity. For both matrix materials, the formation of larger clusters, richer in Ag NPs, is promoted by longer deposition. At a larger observation scale, longer deposition results in thicker coatings and smoother and more homogeneous surface topography. Mechanical characterization reveals that ZrO_2 coatings become stiffer with time, whereas SiO_2 coatings soften due to increased porosity. A general reduction in measurement uncertainty for longer deposition times suggests improved surface uniformity, although ZrO_2 coatings maintain greater variability due to

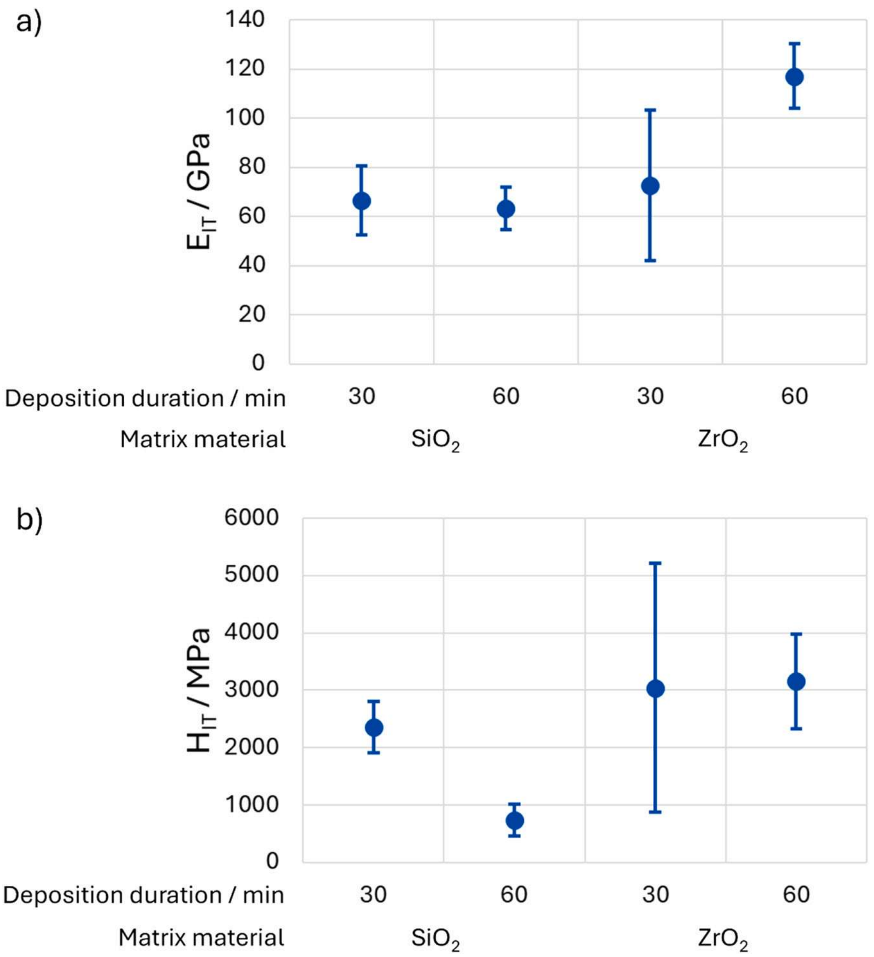

Fig. 8. Nanoindentation mechanical characterization results for the coatings. a) indentation modulus E_{IT}, b) indentation hardness H_{IT} as a function of the matrix material and the deposition duration. Error bars are 95 % confidence intervals.

heterogeneous Ag distribution.

Smoother and more homogeneous surfaces may be advantageous in applications where controlled silver release and surface stability are required. Likewise, the matrix-dependent mechanical response provides guidelines for selecting the most suitable material depending on the target substrate: ZrO_2 is more appropriate for applications requiring higher stiffness, while SiO_2 offers greater compliance for flexible substrates such as textiles and filters.

Overall, the study highlights the tunability of co-sputtered Ag-based composite coatings through process control and provides structure–property relationships that are directly useful for the design of durable, high-performance functional surfaces. Future work will leverage the mechanical results to optimize the design of fibers and textile for antibacterial and antiviral applications.

Author statement

The authors state that the work enclosed has not been published previously, that it is not under consideration for publication elsewhere and that its submission is approved by all the authors.

CRediT authorship contribution statement

Gianfranco Genta: Writing – review & editing, Validation, Formal analysis. **Cristina Balagna:** Writing – review & editing, Supervision, Resources, Project administration, Funding acquisition, Conceptualization. **Maurizio Galetto:** Writing – review & editing, Supervision, Resources, Project administration, Funding acquisition. **Giacomo Maculotti:** Writing – original draft, Visualization, Validation, Methodology, Formal analysis. **Francesca Gattucci:** Writing – original draft, Visualization, Validation, Methodology, Investigation, Data curation. **Lorenzo Giorio:** Writing – original draft, Visualization, Methodology, Investigation, Data curation.

Declaration of Competing Interest

The authors declare that they have no known competing financial interests or personal relationships that could have appeared to influence the work reported in this paper

Acknowledgements

This study was carried out within the MICS (Made in Italy – Circular and Sustainable) Extended Partnership and received funding from the European Union Next-GenerationEU (PIANO NAZIONALE DI RIPRESA E RESILIENZA (PNRR) – MISSIONE 4 COMPONENTE 2, INVESTIMENTO 1.3 – D.D. 1551.11–10–2022, PE00000004). This manuscript reflects only the authors' views and opinions, neither the European Union nor the European Commission can be considered responsible for them.

Data availability

The datasets generated and analyzed during the current study are available from the corresponding authors on reasonable requests.

References

[1] M. Mu, X. Wang, M. Taylor, A. Castillo, L. Cisneros-Zevallos, M. Akbulut, Y. Min, Multifunctional coatings for mitigating bacterial fouling and contamination, Colloid Interface Sci. Commun. 55 (2023) 100717, https://doi.org/10.1016/j.colcom.2023.100717.

[2] E. Christaki, M. Marcou, A. Tofarides, Antimicrobial resistance in bacteria: mechanisms, evolution, and persistence, J. Mol. Evol. 88 (2020) 26–40, https://doi.org/10.1007/s00239-019-09914-3.

[3] S. Baker, N. Thomson, F.-X. Weill, K.E. Holt, Genomic insights into the emergence and spread of antimicrobial-resistant bacterial pathogens, Science 360 (1979) (2018) 733–738, https://doi.org/10.1126/science.aar3777.

[4] W. DeFlorio, S. Liu, A.R. White, T.M. Taylor, L. Cisneros-Zevallos, Y. Min, E.M. A. Scholar, Recent developments in antimicrobial and antifouling coatings to reduce or prevent contamination and cross-contamination of food contact surfaces by bacteria, Compr. Rev. Food Sci. Food Saf. 20 (2021) 3093–3134, https://doi.org/10.1111/1541-4337.12750.

[5] A. Hamad, K.S. Khashan, A. Hadi, Silver nanoparticles and silver ions as potential antibacterial agents, J. Inorg. Organomet. Polym. Mater. 30 (2020) 4811–4828, https://doi.org/10.1007/s10904-020-01744-x.

[6] C. You, C. Han, X. Wang, Y. Zheng, Q. Li, X. Hu, H. Sun, The progress of silver nanoparticles in the antibacterial mechanism, clinical application and cytotoxicity, Mol. Biol. Rep. 39 (2012) 9193–9201, https://doi.org/10.1007/s11033-012-1792-8.

[7] A. Luceri, R. Francese, D. Lembo, M. Ferraris, C. Balagna, Silver nanoparticles: review of antiviral properties, mechanism of action and applications, Microorganisms 11 (2023) 629, https://doi.org/10.3390/microorganisms11030629.

[8] L. Wang, G. Periyasami, A. Aldalbahi, V. Fogliano, The antimicrobial activity of silver nanoparticles biocomposite films depends on the silver ions release behaviour, Food Chem. 359 (2021) 129859, https://doi.org/10.1016/j.foodchem.2021.129859.

[9] Q. Wei, Y. Xu, Y. Wang, Textile surface functionalization by physical vapor deposition (PVD). Surface Modification of Textiles, Elsevier, 2009, pp. 58–90, https://doi.org/10.1533/9781845696689.58.

[10] H. Ichou, N. Arrousse, E. Berdimurodov, N. Aliev, Exploring the advancements in physical vapor deposition coating: a review, J. Bio Tribocorros. 10 (2024) 3, https://doi.org/10.1007/s40735-023-00806-0.

[11] D. Wojcieszak, M. Mazur, D. Kaczmarek, B. Szponar, M. Grobelny, M. Kalisz, A. Pelczarska, I. Szczygiel, A. Poniedzialek, M. Osekowska, Structural and surface properties of semitransparent and antibacterial (Cu,Ti,Nb)Ox coating, Appl. Surf. Sci. 380 (2016) 159–164, https://doi.org/10.1016/j.apsusc.2016.01.232.

[12] M. Ferraris, S. Perero, M. Miola, S. Ferraris, E. Verné, J. Morgiel, Silver nanocluster–silica composite coatings with antibacterial properties, Mater. Chem. Phys. 120 (2010) 123–126, https://doi.org/10.1016/j.matchemphys.2009.10.034.

[13] M. Ferraris, C. Balagna, S. Perero, Wo2019082001 - method for the application of an antiviral coating to a substrate and relative coating, 2017.

[14] M. Irfan, S. Perero, M. Miola, G. Maina, A. Ferri, M. Ferraris, C. Balagna, Antimicrobial functionalization of cotton fabric with silver nanoclusters/silica composite coating via RF co-sputtering technique, Cellulose 24 (2017) 2331–2345, https://doi.org/10.1007/s10570-017-1232-y.

[15] C. Balagna, S. Perero, E. Percivalle, E.V. Nepita, M. Ferraris, Virucidal effect against coronavirus SARS-CoV-2 of a silver nanocluster/silica composite sputtered coating, Open Ceram. 1 (2020) 100006, https://doi.org/10.1016/j.oceram.2020.100006.

[16] A. Luceri, R. Francese, S. Perero, D. Lembo, M. Ferraris, C. Balagna, Antibacterial and antiviral activities of silver nanocluster/silica composite coatings deposited onto air filters, ACS Appl. Mater. Interfaces 16 (2024) 3955–3965, https://doi.org/10.1021/acsami.3c13843.

[17] J. Drewes, N. Perdana, K. Rogall, T. Hartig, M. Elis, U. Schürmann, F. Pohl, M. Abdelaziz, T. Strunskus, L. Kienle, M. Elbahri, F. Faupel, C. Rockstuhl, A. Vahl, Co-sputtering of A thin film broadband absorber based on self-organized plasmonic Cu nanoparticles, Part. Part. Syst. Charact. 41 (2024), https://doi.org/10.1002/ppsc.202300102.

[18] E. Torres Dominguez, P.H. Nguyen, H.K. Hunt, A. Mustapha, Antimicrobial coatings for food contact surfaces: legal framework, mechanical properties, and potential applications, Compr. Rev. Food Sci. Food Saf. 18 (2019) 1825–1858, https://doi.org/10.1111/1541-4337.12502.

[19] H. Wang, Y. Gao, C. Zhang, L. Du, X. Ma, J. Wu, Research progress on implantable medical textiles and their surface functional coatings, J. Polym. Sci. 63 (2025) 1070–1085, https://doi.org/10.1002/pol.20240986.

[20] X. Chen, J. Zhou, Y. Qian, L. Zhao, Antibacterial coatings on orthopedic implants, Mater. Today Bio 19 (2023) 100586, https://doi.org/10.1016/j.mtbio.2023.100586.

[21] J. Plé, M. Dabert, H. Lecoq, S. Hellé, L. Ploux, L. Balan, Antimicrobial and mechanical properties of functionalized textile by nanoarchitectured photoinduced Ag@polymer coating, Beilstein J. Nanotechnol. 14 (2023) 95–109, https://doi.org/10.3762/bjnano.14.11.

[22] S. Mahmoudi-Qashqay, M.-R. Zamani-Meymian, S.J. Sadati, Improving antibacterial ability of Ti-Cu thin films with co-sputtering method, Sci. Rep. 13 (2023) 16593, https://doi.org/10.1038/s41598-023-43875-4.

[23] I. Georgakopoulos-Soares, E.L. Papazoglou, P. Karmiris-Obratański, N.E. Karkalos, A.P. Markopoulos, Surface antibacterial properties enhanced through engineered textures and surface roughness: a review, Colloids Surf. B Biointerfaces 231 (2023) 113584, https://doi.org/10.1016/j.colsurfb.2023.113584.

[24] D. Montgomery, Des. Anal. Exp. (2017).

[25] A. Luceri, S. Perero, A. Cochis, A.C. Scalia, L. Rimondini, M. Ferraris, C. Balagna, Washing resistant antibacterial composite coatings on cotton textiles, Cellulose 30 (2023) 9877–9897, https://doi.org/10.1007/s10570-023-05471-7.

[26] G. Muzio, M. Miola, S. Perero, M. Oraldi, M. Maggiora, S. Ferraris, E. Vernè, V. Festa, F. Festa, R.A. Canuto, M. Ferraris, Polypropylene prostheses coated with silver nanoclusters/silica coating obtained by sputtering: biocompatibility and antibacterial properties, Surf. Coat. Technol. 319 (2017) 326–334, https://doi.org/10.1016/j.surfcoat.2017.03.057.

[27] M. Miola, S. Perero, S. Ferraris, A. Battiato, C. Manfredotti, E. Vittone, D. Del Vento, S. Vada, G. Fucale, M. Ferraris, Silver nanocluster-silica composite antibacterial coatings for materials to be used in mobile telephones, Appl. Surf. Sci. 313 (2014) 107–115, https://doi.org/10.1016/j.apsusc.2014.05.151.

[28] P. de Groot, Phase Shifting Interferometry, in: R.K. Leach (Ed.), Optical Measurement of Surface Topography, Springer-Verlag, Berlin, 2011, pp. 167–186.

[29] ISO 25178-603:2013, Geometrical product specifications (GPS) - surface texture: Areal. Part 603: nominal characteristics of non-contact (phase-shifting interferometric microscopy) instruments, ISO Gen. ève (2013).

[30] ISO 25178-700:2023, Geometrical product specifications (GPS). Surface texture: Areal. Part 700, Calibration. adjustment and verification of areal topography measuring instruments, British Standards Institution, 2023.

[31] ISO 25178-2:2022 Geometrical product specifications (GPS). Surface texture: Areal. Part 2, Terms, definitions and surface texture parameters, British Standards Institution, 2022.

[32] ISO 25178-3:2012 Geometrical product specifications (GPS) — Surface texture: Areal Part 3: Specification operators, (n.d.).

[33] Mountains Map, (n.d.). ⟨www.digitalsurf.com⟩.

[34] D.A. Lucca, K. Herrmann, M.J. Klopfstein, Nanoindentation: measuring methods and applications, CIRP Ann. Manuf. Technol. 59 (2010) 803–819, https://doi.org/10.1016/j.cirp.2010.05.009.

[35] E.S. Puchi-Cabrera, M.H. Staia, A. Iost, Modeling the composite hardness of multilayer coated systems, Thin Solid Films 578 (2015) 53–62, https://doi.org/10.1016/j.tsf.2015.01.070.

[36] ISO 14577-4:2015 Metallic materials - Instrumented indentation test for hardness and materials parameters - Part 4: Test method for metallic and non-metallic coatings, (n.d.).

[37] G. Maculotti, E. Goti, G. Genta, L. Mazza, M. Galetto, Uncertainty-based comparison of conventional and surface topography-based methods for wear volume evaluation in pin-on-disc tribological test, Tribol. Int. 165 (2022) 107260, https://doi.org/10.1016/j.triboint.2021.107260.

[38] G. Maculotti, G. Genta, M. Galetto, An uncertainty-based quality evaluation tool for nanoindentation systems, Measurement 225 (2024) 113974, https://doi.org/10.1016/j.measurement.2023.113974.

[39] JCGM100, Evaluation of measurement data — Guide to the expression of uncertainty in measurement (GUM), Sèvres, France, JCGM (2008), https://doi.org/10.1373/clinchem.2003.030528.

[40] G. Genta, G. Maculotti, Thin coatings thickness measurement by augmented nanoindentation data fusion, CIRP Ann. 73 (2024) 409–412, https://doi.org/10.1016/j.cirp.2024.04.093.

[41] J.I. Goldstein, D.E. Newbury, P. Echlin, D.C. Joy, C.E. Lyman, E. Lifshin, L. Sawyer, J.R. Michael, Scanning Electron Microscopy and X-ray Microanalysis, Springer US, Boston, MA, 2003, https://doi.org/10.1007/978-1-4615-0215-9.